Energy & Environmental Science

Decoupling First-Cycle Capacity Loss Mechanisms in Sulfide Solid-State Batteries

Journal:	*Energy & Environmental Science*
Manuscript ID	EE-ART-10-2024-004908.R1
Article Type:	Paper
Date Submitted by the Author:	27-Nov-2024
Complete List of Authors:	Kaeli, Emma; Stanford University, Materials Science and Engineering; SLAC National Accelerator Laboratory, Applied Energy Division
	Jiang, Zhelong; Stanford University, Materials Science and Engineering; SLAC National Accelerator Laboratory, Applied Energy Division
	Yang, Xiaomian; Stanford University, Materials Science and Engineering
	Choy, Emma; Stanford University, Chemistry; SLAC National Accelerator Laboratory, Applied Energy Division
	Liang, Nicolas; Stanford University, Materials Science and Engineering; SLAC National Accelerator Laboratory, Applied Energy Division
	Barks, Edward; Stanford University, Materials Science and Engineering; SLAC National Accelerator Laboratory, Applied Energy Division
	Wang, Sunny; Stanford University, Chemistry; SLAC National Accelerator Laboratory, Applied Energy Division
	Kang, Stephen; Seoul National University, Department of Materials Science and Engineering; Stanford University, Materials Science and Engineering
	Chueh, William; Stanford University, Materials Science and Engineering; SLAC National Accelerator Laboratory, Applied Energy Division; Stanford University, Energy Science & Engineering

SCHOLARONE™
Manuscripts

Broader Context

Investigating more energy-dense batteries, such as the solid-state battery (SSB), is a critical step to achieving a renewably powered electric vehicle fleet. The solid electrolytes (SEs) employed in SSBs, however, suffer from unwanted oxidation at the interface with the positive electrode, leading to capacity loss and premature battery failure. It is therefore essential to quickly pinpoint the most critical capacity loss mechanisms. Quantifying the relative contributions of loss mechanisms remains elusive due to their parallel, interconnected nature. In this work, we investigate an established sulfide SE using atypical cycling protocols to systematically isolate irreversible and kinetically hindered capacity loss. By quantifying loss mechanisms, we discover a surprisingly high first-cycle Coulombic reversibility, demonstrating that kinetically hindered relithiation of the electrode is often mistaken for a truly irreversible loss. Our findings show that all true irreversibilities stem from the limited reversibility of SE oxidation. Importantly, this work provides a framework for segmenting contributions to redox capacity that can be used to evaluate established and next-generation SEs. This method enables more efficient iteration of new electrolytes, architectures and coatings to improve the viability of SSBs.

Decoupling First-Cycle Capacity Loss Mechanisms in Sulfide Solid-State Batteries

Emma Kaeli[1,2,*], Zhelong Jiang[1,2], Xiaomian Yang[1], Emma P. K. L. Choy[2,3], Nicolas B. Liang[1,2], Edward Barks[1,2], Sunny Wang[2,3], Stephen D. Kang[1,4,*], and William C. Chueh[1,2,5,*]

[1] Department of Materials Science and Engineering, Stanford University, Stanford, CA 94305, USA

[2] Applied Energy Division, SLAC National Accelerator Laboratory, Menlo Park, CA 94025, USA

[3] Department of Chemistry, Stanford University, Stanford, CA 94305, USA

[4] Department of Materials Science and Engineering, Seoul National University, Seoul 08826, Republic of Korea

[5] Department of Energy Science & Engineering, Stanford University, Stanford, CA 94305, USA
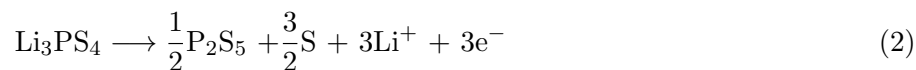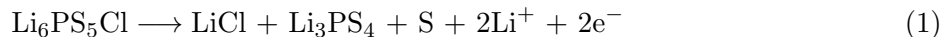
[*] Corresponding author.

Abstract

Solid-state batteries (SSBs) promise more energy-dense storage than liquid electrolyte lithium-ion batteries (LIBs). However, first-cycle capacity loss is higher in SSBs than in LIBs due to interfacial reactions. The chemical evolution of key interfaces in SSBs has been extensively characterized. Electrochemically, however, we lack a versatile strategy for quantifying the reversibility of solid electrolyte (SE) redox for established and next-generation SSB electrolytes. In this work, we perform tailored electrochemical tests and *operando* X-ray diffraction to disentangle reversible and irreversible sources of capacity loss in positive electrodes composed of Li_6PS_5Cl SE, $Li(Ni_{0.5}Mn_{0.3}Co_{0.2})O_2$ (NMC), and carbon conductive additives. We leverage an atypically low voltage cutoff (2.0 V vs. Li/Li^+) to quantify the reversibility of SE redox. Using slow (5.5 mA g_{NMC}^{-1}) cycling paired with > 100 h low-voltage holds, our cells achieve a surprising 96.2% first-cycle Coulombic efficiency, which is higher than previously reported (mean: 72%, maximum: 91.6% across surveyed literature). We clarify that sluggish NMC relithiation kinetics have been historically mistaken for permanently irreversible capacity loss. Through systematic decoupling of loss mechanisms, we uncover the unexpected reversibility of SE redox and iso-

1

late the major contributors to capacity loss, outlining a strategy for an accurate assessment of next-generation SE materials and interface modifications.

1   Introduction

Disentangling parallel capacity loss mechanisms at solid-solid interfaces in solid-state batteries (SSBs) remains a key bottleneck to adoption of this high-density energy storage technology.[1] Layered oxide positive electrodes such as $LiNi_xMn_yCo_zO_2$ (NMC) and $LiNi_xCo_yAl_zO_2$ pair well with mechanically soft solid electrolytes (SEs) to facilitate conformal contact upon compaction.[2] Sulfur-containing SEs, such as Li_3PS_4, $Li_{10}GeP_2S_{12}$, and Li_6PS_5Cl (LPSC), are mechanically compliant and chemically abundant; however, sulfide SEs suffer from oxidative instability with layered oxides at the positive electrode interface.[3] This reactivity, in combination with constriction of ionic and electronic pathways at solid-solid interfaces, leads to high overpotential,[4] parasitic capacity loss,[5] and particle disconnection.[2] Decoupling parallel loss mechanisms enables deterministic evaluation of material modifications, as has been shown in the Si negative electrode of SSBs .[6] This work aims to study the positive electrode and systematically quantify the relative capacity loss contributions of *apparent* (kinetically hindered) irreversibility, such as sluggish SE and NMC redox, and *true* (permanent) irreversibility, such as particle disconnection or path-dependent interfacial reactions.

One loss mechanism, often classified as a *true* irreversibility, is cycling-induced (electrochemical) SE oxidation at the positive electrode interface.[5, 7] During charging, the SE is susceptible to oxidation as the voltage of NMC surpasses 2.3 V vs. Li/Li^+.[5, 8] Specifically, a simplified LPSC reaction pathway includes:

$$Li_6PS_5Cl \longrightarrow LiCl + Li_3PS_4 + S + 2Li^+ + 2e^- \tag{1}$$

$$Li_3PS_4 \longrightarrow \frac{1}{2}P_2S_5 + \frac{3}{2}S + 3Li^+ + 3e^- \tag{2}$$

Although not explicitly included, these decomposition reactions are typically accompanied by intermediate polysulfide products.[9–11] Electrochemically, this SE oxidation is thought to be associated with a 2–5 mAh g_{NMC}^{-1} "shoulder" in the voltage vs. capacity curve at the onset of first-cycle charging (between ~3.0–3.6V vs. Li/Li^+).[12] While evidence shows the relationship between this shoulder

and electrode area,[13, 14] there is not definitive understanding whether the shoulder results from SE oxidation or from other processes that depend on electrode area.

Previous reports suggest that the SE oxidation is permanently irreversible. Cyclic voltammetry is used to determine the voltage stability window for SEs and identify reduction of SE oxidation products;[15] however cyclic voltammetry features conflate the SE reduction current with current generated by the reduction of oxidation products for many common sulfur-containing SEs.[16, 17] Cells cycled galvanostatically using a carbon and SE mixture as the working electrode demonstrate no reversibility when discharged to within the SE voltage stability window, suggesting SE oxidation cannot be reversed.[5, 17] It is still unclear, however, if the SE oxidation is *apparently* irreversible (kinetically hindered) or *truly* (permanently) irreversible under standard cell cycling conditions. The question of SE oxidation reversibility and its impact on SSB performance remains unanswered across established and next-generation SE candidates alike.

In concert with oxidation of the SE at pure electronic conductors (*i.e.*, carbon additives and the current collector), the active material also contributes to *apparently* and *truly* irreversible capacity losses. Layered oxides are prone to releasing oxygen at high voltage.[18] When in contact with layered oxides, LPSC reacts chemically to form Li_3PO_4, $LiCl$, Ni_3S_4 and P_2S_x, and contributes to *truly* irreversible losses due to path-dependent interphase formation.[10, 19, 20] Emergence of oxygen-containing side products is correlated to impedance growth as voltage increases, also contributing to *apparently* irreversible capacity loss.[7, 21] Accompanying interphase formation, layered oxide lattice volume change leads to tenuous solid-solid contacts.[22] Poly-crystalline materials exhibit secondary particle cracking, which results in a greater fraction of ionically or electronically disconnected grains.[22–25] While the interphase chemistry has been studied in detail and electrode microstructure has been optimized to limit constriction,[19, 26–32] quantifying the impact of interphase formation on capacity loss remains a challenge.

Overall, it is more challenging to determine contributions to inefficiency in SSBs than it is in conventional (liquid electrolyte) LIBs.[18] Positive electrode evolution in LIBs is analogous to that in SSBs — LIBs experience liquid electrolyte redox,[33, 34] particle volume change, and cracking. However, electrolyte redox in LIBs results in less-resistive interphase layers and lower apparent irreversible capacity than in SSBs.[34] Additionally, the conformal contact of solid-liquid interfaces in LIBs mitigates contact loss from particle expansion and cracking, resulting in lower active material

loss.[22, 35] These key differences result in a lower magnitude of kinetic and irreversible capacity loss overall, enabling more facile separation of loss mechanisms in LIBs. In SSBs, it is necessary to use longer duration electrochemical measurements and decouple SE redox to accurately compare SSB and LIB performance.

In this work, we use characterize $LiNi_{0.5}Mn_{0.3}Co_{0.2}O_2$ single-crystal positive electrode material behavior with LPSC, a high conductivity ($\sim$1 mS cm^{-1}) SE that undergoes redox within standard cycling windows (oxidation at 2.3 V; reduction at 1.8 V vs. Li/Li$^+$).[11] We investigate the positive electrode, using slow (5.5 mA g$_{NMC}^{-1}$) cycling, 0.5–132 h voltage holds and elevated (45°C) temperatures. By using uncoated NMC, we intentionally encourage the interphase formation with LPSC that we aim to study. Through tailored electrochemical protocols with atypically low voltage cutoffs and *operando* X-ray diffraction (XRD), we present a method for decoupling the reversible, *apparently* irreversible (kinetically hindered), and *truly* irreversible capacity loss mechanisms in SSBs. Our cells achieve a surprising 96.2% first-cycle Coulombic efficiency, which is significantly higher than previously reported.[5, 7, 8, 13, 14, 19, 21, 26–32, 36–76] By quantifying SE oxidation reversibility (27%) we discover that all measurable *truly* irreversible first-cycle capacity loss results from irreversible SE oxidation at pure electronic conductors. Finally, we demonstrate that first-cycle NMC relithiation is severely sluggish and has been incorrectly mislabeled as *truly* irreversible. This work demonstrates a generalizable protocol for assessing loss mitigation strategies in SSBs with established and next-generation SEs prone to oxidation.

2   Results and Discussion

We systematically quantify reversibility of SE oxidation (Section 2.1), *truly* irreversible capacity losses (Section 2.2), and kinetically-limited NMC capacity losses (Section 2.3) to partition first-cycle capacity losses. First, we identified electrochemical indicators connected to capacity loss in the first cycle by comparing voltage curves of LPSC SSBs and carbonate liquid electrolyte LIBs using the same positive electrode components. We use "SSB" and "LIB" conventions to refer to solid and liquid electrolyte batteries, respectively, even though both are lithium-ion batteries. The SSBs use an unlithiated In negative electrode (operated within the two-phase In/InLi region as half cells with no Li reservoir), while the LIBs use a Li negative electrode (half cells with Li reservoir). Cells

were cycled galvanostatically between 2.5–4.3 V at 5.5 mA g_{NMC}^{-1} (C/50, where capacity C=278 mAh g_{NMC}^{-1}) with 10 h top-of-charge and and 33 h bottom-of-discharge voltage holds (Fig. 1a) (see Methods for details; all reported voltages are vs. Li/Li$^+$, and all mass bases are g_{NMC}^{-1}). We begin by quantifying SE oxidation, which has been understood to be a source of *truly* irreversible capacity loss.

2.1 Electrochemical Indicators of First-Cycle Electrolyte Redox

To decouple first-cycle NMC charge capacity from SE oxidation, we compared first-cycle charge and discharge capacity of LIBs and SSBs. We first notice, as expected, that our SSBs exhibit 12.5 ± 1.7% (standard deviation) first-cycle capacity loss, which is greater than LIBs cycled under the same conditions (5.2 ± 1.5%). This difference is expected, in part, due to SE oxidation in SSBs, which inflates the charge capacity. Indeed, in our SSBs charge capacity is inflated by 7.4% above the charge capacity in LIBs (Fig. 1a,b). It is tempting to quantify first cycle SE oxidation capacity as this 7.4%. However, LIBs are likely more delithiated than SSBs at top-of-charge due to an order of magnitude higher impedance in SSBs (Fig. SI-1), making quantifying by direct subtraction inaccurate. Other sources of capacity loss in LIBs, such as solid-electrolyte interphase formation, add to the ambiguity. As we cannot directly compare SSBs and LIBs, we next investigated alternative electrochemical signatures.

To reliably quantify SE oxidation capacity, we instead considered the shoulder at the onset of charging (3–3.6 V) during the first charge. While the SE oxidation voltage is 2.3 V, overpotentials shift the measured shoulder up to the 3–3.6 V range during non-equilibrium cycling. We show the shoulder feature in Fig. 1c, which is associated with 3.6 ± 0.6 mAh g^{-1} capacity. Typical protocols use discharge voltage cutoffs above the 2.3 V SE redox potential; as a result, SE oxidation is not reversed, and indeed the shoulder does not reappear on the second cycle, providing evidence of SE oxidation. We do not expect the shoulder capacity to represent the total SE oxidation, let alone *all* first cycle capacity losses, for several reasons. First, SE oxidation could occur over a broad voltage range above the measured 3–3.6 V shoulder voltage range. Employing even slower cycling via galvanostatic-intermittent titration technique (GITT), Fig. SI-2, demonstrates that with 24 h rests after pulsing, quasi-open circuit conditions (voltage relaxation < 1 mV/h) could not be achieved due to sluggish SE oxidation kinetics. Therefore the SE oxidation extracted from the shoulder in
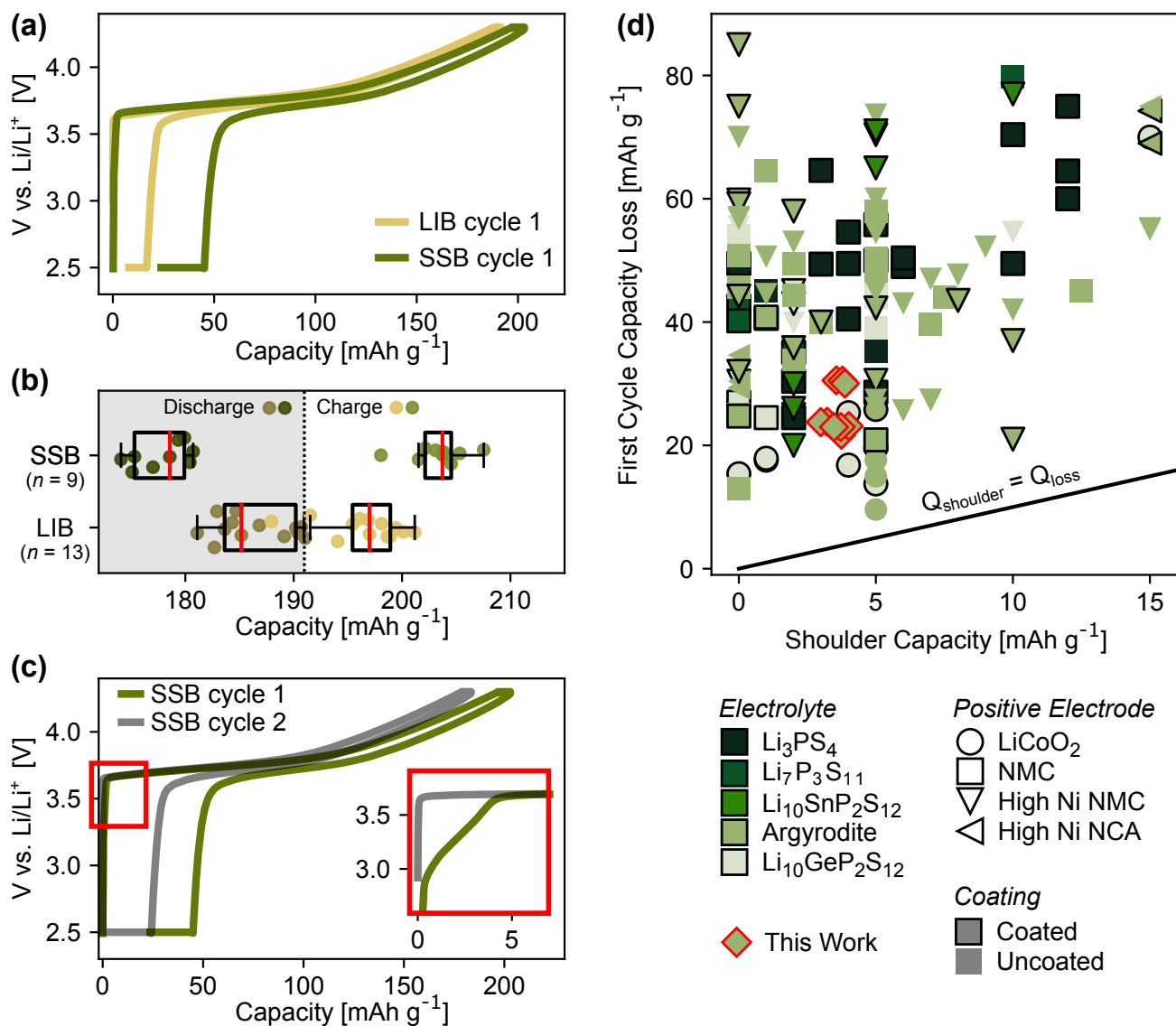
5

Figure 1: **First-cycle voltage curves show inflated charge capacity and a shoulder feature related to SE oxidation in SSBs.** (a) First-cycle SSB and LIB voltage curves and (b) total capacities, show an increase in SSB charge capacity and decrease SSB in discharge capacity (box plots, where red lines indicate median, box indicates middle 50% of data, whiskers represent the upper and lower 25% of data). (c) First and second cycle voltage curves for SSBs show a 2–5 mAh g^{-1} SE oxidation shoulder that appears for only the first cycle (inset shows initial charging portion of voltage vs. capacity curve of cycle 1 and 2). (d) First-cycle capacity loss vs. width of the charging onset shoulder from our data ($\diamond$) and literature[5, 7, 8, 13, 14, 19, 21, 26–32, 36–76] reveals that first-cycle capacity loss is greater than shoulder capacity.

GITT (8.9% of first cycle charge capacity) represents an underestimation. The kinetically-favored NMC oxidation leads to a higher mixed potential despite slow cycling conditions and available SE oxidation capacity at 2.3 V. As a result, the non-equilibrium shoulder feature may not represent all SE oxidation, which may occur at higher voltages. Second, additional kinetic or *truly* irreversible loss mechanisms will add to the total first-cycle losses. Nevertheless, as the shoulder does not persist past the first cycle, we argue that shoulder capacity is simply a measure of the *minimum* capacity loss possible on the first cycle.

Accordingly, we expect the minimum first-cycle capacity loss to be related to the shoulder width in cycling data. The first-cycle capacity loss we measure (25.5 ± 6.8 mAh g^{-1}, or 12.5% of first-cycle charge capacity, from Fig. 1b) is, as expected, greater than our 3.6 mAh g^{-1} shoulder capacity (Fig. 1d). Our results are consistent with literature[5, 7, 8, 13, 14, 19, 21, 26–32, 36–76] as we find that first-cycle capacity loss is always equal to or greater than shoulder capacity. Combining our data with literature results, we demonstrate that the shoulder is a reliable indicator of the minimum losses due to SE oxidation. Using this indicator, we determined the scaling relationship between the shoulder and the total SE oxidation capacity during first-cycle charge.

To eliminate contributions from NMC capacity and isolate SE oxidation at pure electronic conductor interfaces, we constructed composite electrodes with only carbon and SE using identical SE:carbon ratios as in NMC-containing cells (Fig. 2). The capacity calculated in Fig. 2 uses a g$_{\mathrm{NMC}}^{-1}$ basis, representing the mass of NMC a carbon-only cell would theoretically contain if NMC had been included in the electrode. We investigated shoulder capacity and SE oxidation reversibility by explicitly controlling the voltage curve to mimic voltage vs. time (Fig. 2a) profiles derived from NMC-containing cells. By exposing the carbon-SE interface to the same voltages it would encounter in NMC-containing cells for the same amount of time, we estimate the proportion of SE oxidation that occurs *before* and *after* the shoulder is complete.

We used our carbon-only cell data to determine the relationship between shoulder capacity and total first-cycle SE oxidation capacity. By quantifying the charge capacity within the shoulder's voltage window < 3.6 V, $Q_{\mathrm{SE\ ox,\ }<3.6V}^{\mathrm{carbon\text{-}only}}$ (Fig. 2b), we estimated the extent of SE oxidation completion. We note that by removing NMC, we change the total surface area of SE with all electronic conductors. To avoid inaccuracies resulting from the changing surface area, we extract the *fraction* of first-cycle SE oxidation capacity that occurs during the shoulder, rather than absolute value of
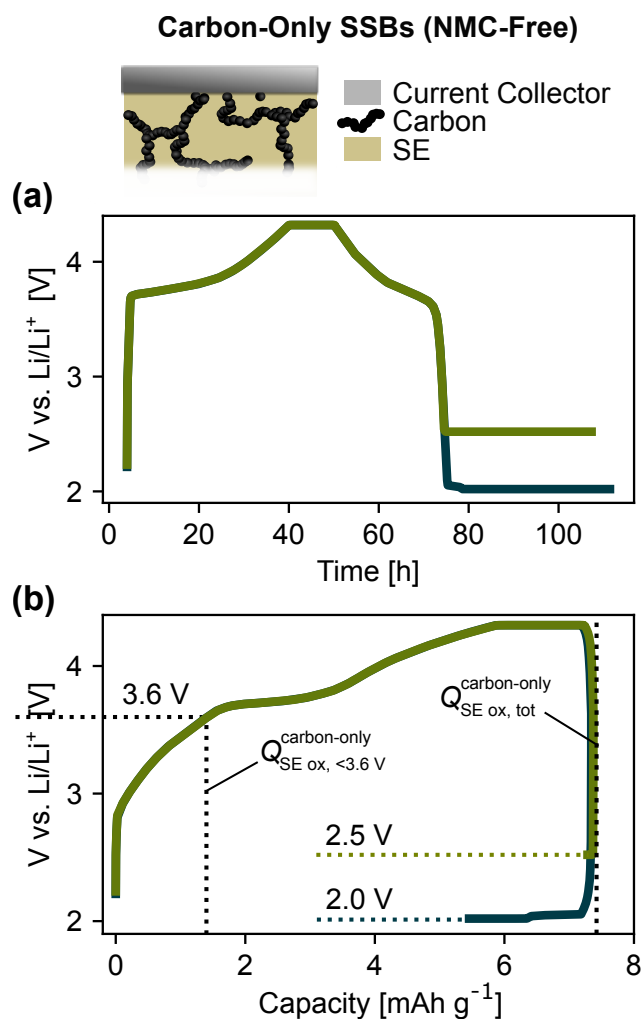
Figure 2: **Quantifying SE oxidation and its reversibility with cells constructed with only carbon and SE.** (a) Voltage vs. time curves and the resulting (b) voltage vs. capacity curves for cells constructed with a carbon | SE electrode, cycled using the voltage vs. time profile extracted from NMC-containing cells, discharged to 2 (navy) or 2.5 V (green).

SE oxidation capacity. As shown in Fig. SI-3, for carbon-only cells in which we intentionally vary the carbon to SE surface area, we find this fraction is invariant to changing surface area. Comparing $Q_{\text{SE ox, }<3.6V}^{\text{carbon-only}}$ to total SE oxidation capacity ($Q_{\text{SE ox, tot}}^{\text{carbon-only}}$, the maximum charge capacity up to 4.3 V), we found that the shoulder capacity represents only 18.9% of total SE oxidation. We then used this fraction to estimate total SE oxidation in our NMC-containing cells using the measured shoulder capacity from NMC-containing cells ($Q_{\text{shoulder}}^{\text{NMC cont.}}$ / $Q_{\text{SE ox, tot}}^{\text{NMC cont.}}$ ~ $Q_{\text{SE ox, }<3.6V}^{\text{carbon-only}}$ / $Q_{\text{SE ox, tot}}^{\text{carbon-only}}$ = 18.9%). For our measured first-cycle shoulder, 3.6 mAh g^{-1} (Fig. 1d) and charge capacity, 203.3 mAh g^{-1} (Fig. 1b), we estimate that SE oxidation accounts for approximately 9.4% of first-cycle charge capacity $\left(Q_{\text{SE ox, tot}}^{\text{NMC cont.}} \middle/ Q_{\text{chg}}^{\text{NMC cont.}} = \frac{3.6 \text{ mAh g}^{-1}}{(18.9\%)\left(203.3 \text{ mAh g}^{-1}\right)} = 9.4\% \right)$. With our estimate of SE oxidation capacity, we then quantified the reversibility of SE oxidation to understand what *truly* irreversible losses stem from SE oxidation.

To quantify the SE oxidation reversibility in carbon-only cells, we used an atypically low (2.0-V) and long duration (33 h) discharge voltage hold. By using a voltage hold within the stability window of the SE (1.8–2.3 V), we aimed to reduce only the SE oxidation products (*i.e.*, reverse Eqs. 1 and 2) without reducing LPSC further. We refer here to "SE oxidation" and "reduction of SE oxidation products" as "SE redox", excluding reduction of pristine SE. Discharging carbon-only cells to 2.0 V and implementing a 33 h voltage hold enables partial recovery of first-cycle SE oxidation capacity on discharge (Fig. 2b). We observe that cells discharged and held at 2.5 V by contrast do not recover discharge capacity, as expected. With the 2.0-V discharge hold, the SE oxidation capacity is only $27 \pm 1\%$ reversible, indicating SE oxidation at the interface with pure electronic conductors accounts for a portion of first-cycle *truly* irreversible capacity loss in NMC-containing cells.

2.2 Quantified Total *Truly* Irreversible Capacity Loss

With our understanding of the contribution of SE redox to first-cycle capacity loss, we used the same low-voltage protocols to more accurately quantify total *truly* irreversible capacity loss in NMC-containing SSB cells. By making use of our atypically low 2.0-V discharge voltage hold, we delivered a higher driving force for both SE redox and relithiation of NMC. The SSBs held at 2.0 V recover 5% more discharge capacity in comparison to those held at 2.5 V (Fig. 2a). It is once again tempting to ascribe all regained discharge capacity to reversed SE oxidation; however, NMC relithiation is also impacted by the lower voltage cutoff. Thus, the improved cell reversibility

9

achieved via the 2.0-V hold can be attributed to both continued relithiation of NMC and reduction of SE oxidation products.

To determine the maximum first-cycle reversibility in our SSB cells, we varied the 2.0-V hold duration on cycle 1 discharge and measured Coulombic efficiency (discharge capacity $Q_{\text{dis},1}$ divided by charge capacity $Q_{\text{chg},1}$) (Fig. 3b). As expected, the Coulombic efficiency increases with voltage hold duration. We find that the SSB achieves a surprising 96.2% Coulombic efficiency with a 66 h voltage hold (cycling data in Fig. SI-4), higher than previously reported: 72% average across reports, 91.6% maximum[14] (Fig. 1d). In comparison, our cells achieve only $87.5 \pm 1.7\%$ Coulombic efficiency with the 2.5-V hold (Fig. 1b). Achieving 3.8% *truly* irreversible first-cycle capacity losses for hold times $\geq$ 66 h demonstrates that SSB first-cycle capacity is, counter to previous understanding, mostly reversible, albeit kinetically limited.

We then verified that non-NMC redox capacity regained via the low voltage hold does not result from a different, non-passivating reduction reaction, such as reduction of the original SE. Extending the duration of the voltage hold past 66 h does not increase the Coulombic efficiency beyond 96.2% (Fig. 3b). Because the upper bound is below 100%, we confirm that capacity arises solely from reduction of SE oxidation products and NMC relithiation.

2.3　Apparent Irreversible Capacity from Sluggish NMC Relithiation

Next, we distinguished NMC redox from SE redox by examining the shoulder behavior on the subsequent cycle. After discharging to 2.0 V on cycle 1, we find that cycle 2 is marked by a reappearance of the SE oxidation shoulder (Fig. SI-5), which does not occur for cells discharged to 2.5 V for any duration. We extracted the capacity of the cycle 2 SE oxidation shoulder ($Q_{\text{shoulder},2}$) and show that $Q_{\text{shoulder},2}$ increases with voltage hold duration (Fig. 3c, legend indicates voltage hold duration). This, along with our quantification of SE oxidation, enables us to use $Q_{\text{shoulder},2}$ as an indicator for the total SE oxidation capacity. Therefore, we examined the correlation between $Q_{\text{shoulder},2}$ (normalized to $Q_{\text{chg},1}$) and Coulombic efficiency ($Q_{\text{dis},1}/Q_{\text{chg},1}$) to distinguish reduction of SE oxidation products from NMC relithiation during first-cycle discharge (Fig. 3c). If NMC relithiation dominates any portion of the discharge process, we would see Coulombic efficiency increase without increase in $Q_{\text{shoulder},2}$. At 45°C, SE redox occurs throughout the voltage hold as $Q_{\text{shoulder},2}$ correlates with Coulombic efficiency. Although we confirm SE redox occurs during
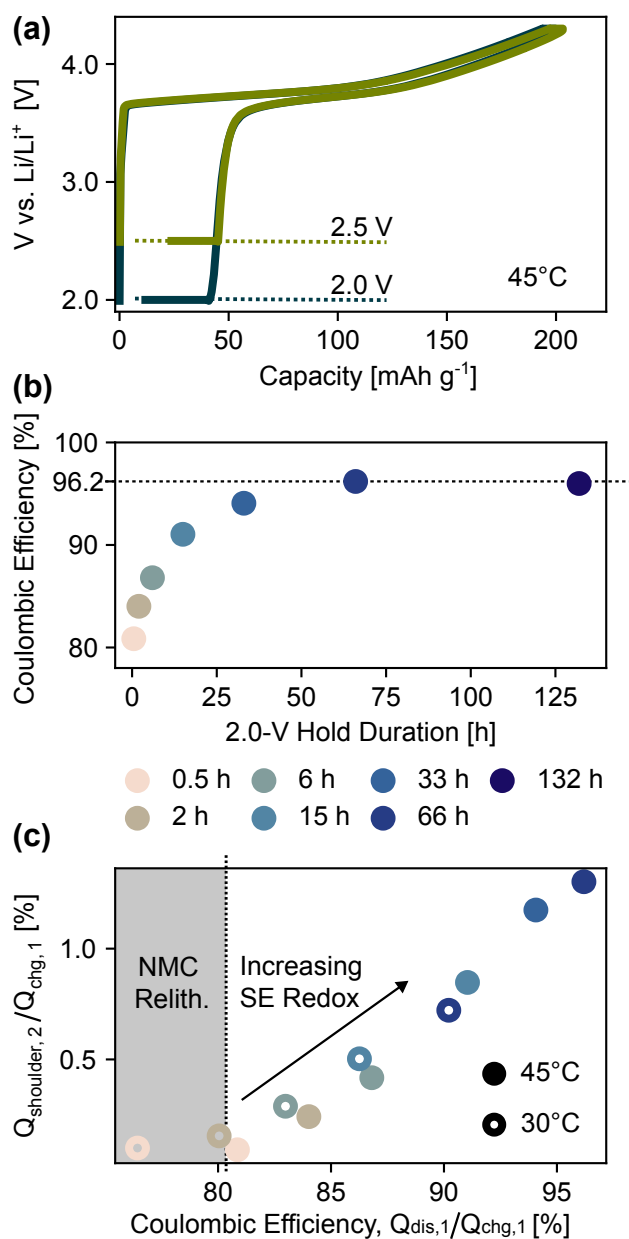
10

Figure 3: **Quantifying _truly_ irreversible losses by reversing SE oxidation.** (a) Voltage vs. capacity curves comparing SSBs with 2.5-V (green) and 2.0-V (navy) discharge voltage holds. (b) Cycle 1 Coulombic efficiency (discharge capacity $Q_{\mathrm{dis},1}$ divided by charge capacity $Q_{\mathrm{chg},1}$) as a function of 2.0-V discharge voltage hold duration. Voltage hold duration 66 h results in 3.8% total Coulombic irreversibility, and duration > 66 h does not recover additional capacity. (c) Normalized cycle 2 shoulder capacity ($Q_{\mathrm{shoulder},2}/Q_{\mathrm{chg},1}$) compared to Coulombic efficiency for cells at 30°C and 45°C with varied 2.0-V discharge hold duration. Limited growth of $Q_{\mathrm{shoulder},2}$ as a function of Coulombic efficiency indicates SE oxidation products were not reduced in cycle 1, as indicated by shaded region.

first-cycle discharge via the second-cycle shoulder, it is difficult to distinguish SE redox from NMC relithiation at higher temperatures.

We repeated our long voltage hold experiment on our SSBs at a lower temperature (30°C) during later cycles to exacerbate resistance and probe sluggish NMC relithiation kinetics (see Methods). Higher resistance leads to increased overpotentials, so the SSB reaches the 2.0-V cutoff at a lower extent NMC relithiation (Fig. SI-6). We predicted that the fraction of the 2.0-V hold capacity that arises from NMC relithiation capacity will be larger at 30°C than at 45°C. As shown in Fig. 3c, we observe that for 30°C cells with Coulombic efficiency < 80%, there is minimal growth in $Q_{\text{shoulder},2}$ as Coulombic efficiency increases. This trend indicates that earlier in the discharge process during the 2.0-V hold, NMC relithiation predominates. Thereafter, $Q_{\text{shoulder},2}$ increases with Coulombic efficiency as in the 45°C cells. While reduction of SE oxidation products is thermodynamically allowed below 2.3 V vs. Li/Li$^+$, we find it is kinetically limited when NMC relithiation is favored. As a result, we discover that NMC relithiation precedes the onset of SE redox during discharge, and NMC relithiation becomes a more substantial contributor to kinetically-limited capacity loss at lower temperatures.

The kinetically hindered capacity losses from NMC were confirmed via *operando* XRD during discharge (Fig. 4a-c) at room temperature. By tracking the (003) diffraction peak of NMC, we confirm that first-cycle NMC relithiation continues throughout the 2.0-V voltage hold. Due to limitations of the measurement, cells were cycled at an even lower temperature, 25°C. Taken together, these findings demonstrate the impact high SSB cell impedance has on performance — lower temperatures impart sluggish NMC relithiation kinetics in SSBs, which can be mistaken for *truly* irreversible capacity loss.

2.4   Decoupled First-Cycle Capacity Loss Contributions

Taken together, our findings enable us to estimate the relative contributions of first-cycle capacity loss mechanisms, as summarized in Fig. 5a:

- In total, for our NMC-containing SSB cells with a 33 h 2.5-V hold, we achieved **87.5 ± 1.7% practically reversible capacity** (Fig. 1b) when cycling cells at 45°C, resulting in 12.5% first-cycle capacity loss.
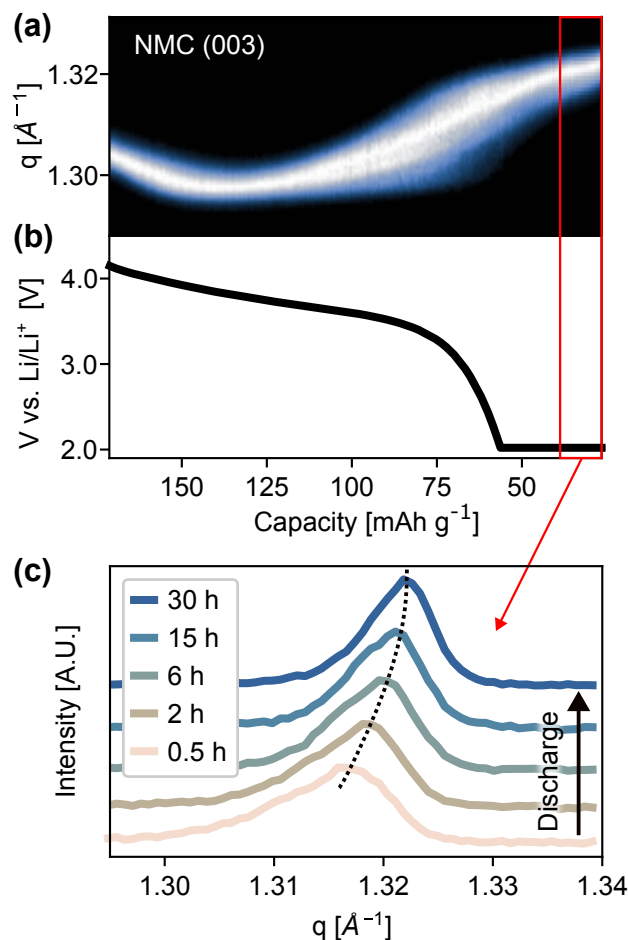
Figure 4: **Confirming kinetic losses via *operando* XRD.** (a) *operando* XRD patterns for the (003) peak of NMC and (b) voltage vs. capacity curve for discharging SSB at room temperature. (c) Individual patterns during end of voltage hold for (003) peak of NMC (dashed guide line shows NMC peak position).

- Using the fraction of first-cycle SE oxidation capacity represented by the shoulder (extracted from our carbon-only cells, shown in Fig. 2b), we estimated that 9.4% of charge capacity in NMC-containing cells comes from SE oxidation; subtracting this from the 12.5% first-cycle capacity loss, we find **3.1% of first-cycle capacity is lost to kinetically-hindered NMC relithiation.**

- Cells held for at least 66 h at 2.0 V demonstrate that first-cycle capacity is surprisingly 96.2% reversible, or only **3.8% *truly* irreversible** (Fig. 3b).

- Our carbon-only cells (Fig. 1b) also reveal the limited Coulombic reversibility of SE oxidation at the interface with pure electronic conductors (27% reversibility for 33 h, 2.0-V discharge

13

hold). We can therefore ascribe all **3.8% first-cycle *true* irreversibility to irreversible SE oxidation**.

- Finally, by subtracting the 3.8% *truly* irreversible losses from the 9.4% of first-cycle capacity lost to SE oxidation, we determine that **5.6% of first-cycle capacity is reversible SE oxidation**.
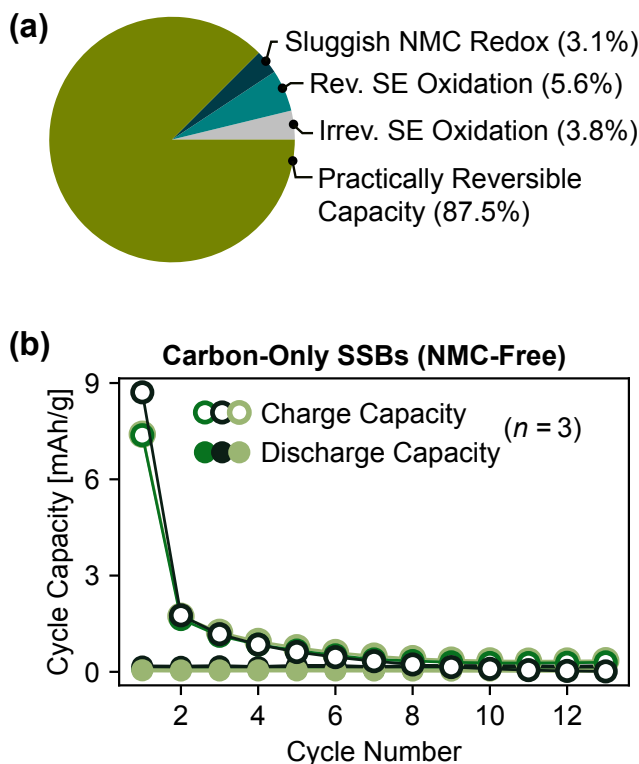

Figure 5: **Decoupled capacity loss mechanisms for first cycle and beyond.** (a) Decoupled first-cycle capacity loss contributions. (b) Charge and discharge capacities past the first cycle in carbon-only cells ($n = 3$ replicates shown) cycled between 2.5–4.3 V, showing oxidation capacity persisting past the first cycle.

Combining all of our measurements enables us to quantify capacity loss and decouple the mechanisms (Fig. 5a). We note that our estimations based on carbon-only cells would suggest 6.8% of first-cycle capacity is *truly* irreversible (only 27% of the 9.4% charge capacity from SE oxidation was estimated to be reversible). The 6.8% estimate from carbon-only cells is larger than the 3.8% *true* irreversibility we measure in NMC-containing cells; however, we note the 6.8% carbon-only estimate is measured via a 33 h 2.0-V discharge hold, while the 3.8% estimate from NMC-containing cells is measured via a 66 h 2.0-V discharge hold. If we examine NMC-containing cells that only

use a 33 h 2.0-V discharge hold, however, we find they exhibit 6.0% irreversibility, which is similar to the 6.8% estimate from the 33 h carbon-only cells. The carbon-only cells were not tested beyond a 33 h voltage hold, but we speculate a similar *true* irreversibility estimate would be derived for long (66 h+) voltage holds. Further, because partial irreversibility of SE oxidation likely accounts for all first-cycle *true* irreversibility, we argue that other *truly* irreversible loss mechanisms, such as particle disconnection or SE redox involving NMC, do not account for measurable first-cycle capacity loss. By decoupling these loss mechanisms, we discovered partial SE oxidation reversibility, a higher total reversibility, and key limitations in SSB cycling.

2.5   Electrolyte Oxidation Beyond the First Cycle

With the loss mechanisms decoupled, we used the same electrochemical approaches to track capacity loss and SE oxidation during early-life aging. Throughout literature, cells discharged to 2.5 V on the first cycle do not exhibit a shoulder on subsequent cycles, so it is broadly assumed that SE oxidation occurs only on the first cycle. However, cells containing NMC exhibit ~99% Coulombic efficiency past the first cycle (Fig. SI-7). Although 99% is significantly higher than the surveyed literature average (72%) first-cycle Coulombic efficiency, the remaining $\sim 1\%$ Coulombic inefficiency remains unattributed to a specific mechanism, and leads to long-term capacity fade. To investigate the residual Coulombic inefficiency, we cycled our carbon-only cells without reducing SE oxidation products and measured capacity past the first cycle. Contrary to existing understanding, our carbon-only cells exhibit SE oxidation (charge) capacity beyond the first cycle (Fig. 5b). Although the magnitude of the SE capacity is small, 18% of the first cycle's capacity on cycle 2, its persistence indicates that SE oxidation continues past the first cycle. This overlooked capacity loss mechanism therefore contributes to long-term capacity loss in the SSB cells.

3   Conclusions

We demonstrate a method for decoupling the reversible, apparently irreversible (kinetically hindered), and *truly* irreversible capacity loss mechanisms in SSBs. By combining long-timescale electrochemistry, carbon-only NMC-free electrodes, and *operando* XRD, we show that SSB first-cycle capacity is reversible up to 96.2%, which is substantially higher than previously reported.

Upon isolating SE redox from NMC cycling, we find redox at the interface between SE and pure electronic conductors is only 27% reversible. Taken together, the 3.8% first-cycle loss in the NMC-containing cell likely stems from irreversible SE oxidation at pure electronic conductor interfaces. Therefore, other irreversible loss mechanisms, such as particle disconnection or SE redox involving NMC, do not account for measurable capacity loss. We demonstrate the severe impact of sluggish NMC relithiation kinetics on capacity loss near room temperature; in doing so, we discover that reduction of SE oxidation products only begins after NMC relithiation has achieved 80% Coulombic efficiency during the discharge voltage hold. While the quantification we have done applies only to our cell composition, our decoupling method represents a generalizable strategy that researchers can apply to their own cell compositions and architectures to assess reversibility and relative loss mechanism contributions. Considered together, these findings complement the existing chemical understanding of high impedance interphase layers by quantifying the first-cycle capacity loss from sluggish NMC relithiation.

With the capacity contributions decoupled, we reveal the relationship between SE oxidation and performance past the first cycle. Notably, we show that SE oxidation persists beyond the first cycle in SSBs. This analysis demonstrates the utility of decoupling capacity loss mechanisms, enabling us to explore useful metrics and measurements for tracking degradation in batteries.

4   Methods

4.1   Materials

Single-crystal $LiNi_{0.5}Mn_{0.3}Co_{0.2}O_2$ (NMC-532) was acquired from Microvast and stored in an Ar-containing glovebox (< 1 ppm H_2O and O_2). We used single-crystal to eliminate the kinetic limitations incurred from polycrystal particle cracking. Li_6PS_5Cl (LPSC) powders were obtained from NEI Corporation. Indium foil (1.0 mm thick, 99.996.2% purity) was purchased from Thermo Fisher Scientific. TIMCAL Carbon Super-P was obtained from MSE Supplies.

4.2 Electrochemical Measurements

4.2.1 SSB Cell Fabrication

All cell preparation was performed in an Ar-containing glovebox ($<$ 1 ppm H_2O and O_2). The composite positive electrode (60% NMC, 35% LPSC, 5% carbon by mass) was made by hand grinding with an agate mortar and pestle. NMC and carbon powder were dried under active vacuum under 12 mbar at 250°C and 300°C, respectively, for 24 hours (Büchi Glass Oven B-585). First, LPSC and NMC powders were combined and mixed for 12 minutes. Carbon was added and mixed again for 12 minutes. For carbon-only cells, 12.5% carbon and 87.5% LPSC by mass were combined via the same method. Solid-state batteries (SSBs) were built using custom-designed parts. The solid electrolyte (SE) pellet was formed into 1 mm thick pellet using a 10 mm PEEK die under 30 MPa compaction. The composite positive electrode mixture was added (11.5 mg_{NMC} cm^{-2} loading) and the entire pellet was compacted to 360 MPa. For carbon-only cells, composite carbon|LPSC mixture was added such that the mass of LPSC+C in NMC-containing cells matched that of the carbon-only cells. A disc of 9 mm indium foil was attached to the reverse side of the pellet.

4.2.2 SSB Cell Electrochemical Testing

Cells used stainless steel current collectors enclosed in an aluminum pouch to enable cycling outside of the glovebox environment. Operating pressure (18 MPa) was applied externally with steel plates. All cell tests were performed at 45°C to achieve greater capacity extraction at shorter timescales. Standard cycling tests were performed on Biologic BCS-805 potentiostats at C/50 (C=278 mAh g_{NMC}^{-1}) between 2.0 V or 2.5 V and 4.3 V vs. Li/Li^+, with a 10 h voltage hold at top of charge and a 33 h voltage hold at bottom of discharge unless otherwise stated. Potentiostatic electrochemical impedance spectroscopy was collected from 10 kHz to 100 mHz with a voltage amplitude of 3-10 mV after 5 minutes open circuit rest.

We note that the same SSBs were used for the 45°C (cycles 1 and 2) and 30°C (cycles 5 and 6) 2.0-V hold duration tests. The referenced $Q_{dis,1}$ and $Q_{shoulder,2}$ for 30°C cells in Fig. 5 refer to results from cycles 5 and 6, respectively, but are labeled as cycle 1 and 2 for ease of explanation. All data is normalized to cycle 1 charge capacity ($Q_{chg,1}$) for accurate comparison. Cells cycled

17

with shorter cycle 1 discharge voltage holds were cycled with longer cycle 5 discharge voltage holds (and vice versa) to prevent any carryover from cycle 1 effects. We note that cycle aging does not impact the resulting findings, as long-term cycling using 2.0-V discharge holds (Fig. SI-8) shows that the voltage drop during discharge occurs at higher discharge capacities due to cycle aging, whereas cycling at 30°C shows the opposite effect, despite cycle aging (Fig. SI-6).

4.2.3   LIB Cell Fabrication and Electrochemical Testing

Lithium-ion battery (LIB) positive electrode sheets were prepared via mixing PVDF, NMC and carbon (7.5%, 85%, 7.5% by mass) with N-methylpyrrolidone (Sigma Aldrich) and coating in air on carbon-coated aluminum foil at 100 μm using a doctor blade. The electrode sheet was dried at 60°C for 12 hours and stored in an Ar-containing glovebox. Electrodes were punched to 1 cm^2 area and used to build stainless steel coin cells with Celgard separator, Li foil counter electrode, and 1 M LiPF$_6$ EC/DEC electrolyte (LP40, E-lyte Innovations). Cycling conditions were the same as for SSBs unless otherwise stated.

4.3   X-ray Diffraction

X-ray diffraction (XRD) was performed at Stanford Synchrotron Radiation Lightsource Beamline 2-1 (17 keV). For SSBs, pellets were removed from the PEEK die they were pressed in prior to attaching a thin (150 μm) indium counter electrode. Copper and aluminum foil were used as current collectors. The cells were sealed in an aluminum pouch and pressurized with steel plates with an embedded beryllium window. Cells were charged at C/30 (C=278 mAh g$_{\mathrm{NMC}}^{-1}$) with 1 h and 33 h voltage holds at top of charge (4.3 V vs. Li/Li$^+$) and bottom of discharge (2.0 V vs. Li/Li$^+$). Cells were operated at room temperature due to limitations of the measurement conditions, around 20—25°C.

Author Contributions

E. K., S. D. K. and W. C. C. formulated the project goals and research plan. W. C. C. and S. D. K. supervised the work. E. K. performed the electrochemical measurements. E. K. and Z. J. performed the *operando* XRD measurements. E. K. and X. Y. optimized the cell fabrication procedure. E.

K. and E. P. K. L. C. performed X-ray photoelectron spectroscopy measurements used to guide the project direction. N. B. L. assembled LIB cells for *operando* XRD measurements used to guide the project direction. E. B. designed and fabricated in-house cell parts. S. W. contributed to data analysis. All authors discussed the results and contributed to preparing the final draft of the manuscript.

Conflicts of interest

There are no conflicts to declare.

Data Availability

Data for this article, including the electrochemistry and X-ray diffraction data shown here, is available at Harvard Dataverse at `https://doi.org/10.7910/DVN/RET3CV`.

Acknowledgements

and for their helpful discussion and comments on the manuscript.

References

1. Miao X, Guan S, Ma C, Li L, and Nan CW. Role of Interfaces in Solid-State Batteries. Advanced materials 2023.

2. Farzanian S, Vazquez Mercado J, Shozib I, et al. Mechanical Investigations of Composite Cathode Degradation in All-Solid-State Batteries. ACS Applied Energy Materials 2023;6:9615–23.

3. Wang C, Liang J, Zhao Y, Zheng M, Li X, and Sun X. All-solid-state lithium batteries enabled by sulfide electrolytes: From fundamental research to practical engineering design. Energy & environmental science 2021;14:2577–619.

4. Yu CY, Choi J, Dunham J, et al. Time-resolved impedance spectroscopy analysis of aging in sulfide-based all-solid-state battery full-cells using distribution of relaxation times technique. Journal of power sources 2024;597.

5. Banerjee A, Tang H, Wang X, et al. Revealing Nanoscale Solid-Solid Interfacial Phenomena for Long-Life and High-Energy All-Solid-State Batteries. ACS applied materials & interfaces 2019;11:43138–45.

6. Tan DHS, Chen YT, Yang H, et al. Carbon-free high-loading silicon anodes enabled by sulfide solid electrolytes. Science 2021;373:1494–9.

7. Hu X, Zhao Z, Zhao Y, et al. Interfacial degradation of the NMC/Li6PS5Cl composite cathode in all-solid-state batteries. Journal of materials chemistry. A, Materials for energy and sustainability 2024;12:3700–10.

8. Zuo TT, Walther F, Teo JH, et al. Impact of the Chlorination of Lithium Argyrodites on the Electrolyte/Cathode Interface in Solid-State Batteries. Angewandte Chemie - International Edition 2023;62.

9. Richards WD, Miara LJ, Wang Y, Kim JC, and Ceder G. Interface Stability in Solid-State Batteries. Chemistry of materials: a publication of the American Chemical Society 2016;28:266–73.

10. Teo JH, Strauss F, Walther F, et al. The interplay between (electro)chemical and (chemo)mechanical effects in the cycling performance of thiophosphate-based solid-state batteries. Materials Futures 2022;1.

11. Banik A, Liu Y, Ohno S, et al. Can Substitutions Affect the Oxidative Stability of Lithium Argyrodite Solid Electrolytes? ACS Applied Energy Materials 2022;5:2045–53.

12. Ohta N, Takada K, Zhang L, Ma R, Osada M, and Sasaki T. Enhancement of the high-rate capability of solid-state lithium batteries by nanoscale interfacial modification. Advanced materials 2006;18:2226–9.

13. Zhang W, Leichtweiß T, Culver SP, et al. The Detrimental Effects of Carbon Additives in Li10GeP2S12-Based Solid-State Batteries. ACS applied materials & interfaces 2017;9:35888–96.

14. Park SW, Oh G, Park JW, et al. Graphitic Hollow Nanocarbon as a Promising Conducting Agent for Solid-State Lithium Batteries. Small 2019;15.

15. Swamy T, Chen X, and Chiang YM. Electrochemical Redox Behavior of Li Ion Conducting Sulfide Solid Electrolytes. Chemistry of materials: a publication of the American Chemical Society 2019;31:707–13.

16. Dewald GF, Ohno S, Kraft MA, et al. Experimental Assessment of the Practical Oxidative Stability of Lithium Thiophosphate Solid Electrolytes. Chemistry of materials: a publication of the American Chemical Society 2019;31:8328–37.

17. Tan DHS, Wu EA, Nguyen H, et al. Elucidating reversible electrochemical redox of Li_6PS_5cl solid electrolyte. ACS energy letters 2019;4:2418–27.

18. Zhang H, Liu H, Piper LFJ, Whittingham MS, and Zhou G. Oxygen Loss in Layered Oxide Cathodes for Li-Ion Batteries: Mechanisms, Effects, and Mitigation. Chemical reviews 2022;122:5641–81.

19. Zuo TT, Walther F, Ahmed S, et al. Formation of an Artificial Cathode-Electrolyte Interphase to Suppress Interfacial Degradation of Ni-Rich Cathode Active Material with Sulfide Electrolytes for Solid-State Batteries. ACS Energy Letters 2023;8:1322–9.

20. Wang Z, Wang Z, Xue D, et al. Reviving the rock-salt phases in Ni-rich layered cathodes by mechano-electrochemistry in all-solid-state batteries. Nano Energy 2023;105.

21. Zuo TT, Rueß R, Pan R, et al. A mechanistic investigation of the Li10GeP2S12— LiNi1-x-yCoxMnyO2 interface stability in all-solid-state lithium batteries. Nature communications 2021;12:6669.

22. Zhang X, Wang Z, Li X, et al. Assessing the roles of mechanical cracks in Ni-rich layered cathodes in the capacity decay of liquid and solid-state batteries. Materials Horizons 2023;10:1856–64.

23. Lee S, Su L, Mesnier A, Cui Z, and Manthiram A. Cracking vs. surface reactivity in high-nickel cathodes for lithium-ion batteries. Joule 2023;7:2430–44.

24. Ruess R, Schweidler S, Hemmelmann H, et al. Influence of NCM Particle Cracking on Kinetics of Lithium-Ion Batteries with Liquid or Solid Electrolyte. Journal of the Electrochemical Society 2020;167:100532.

25. Perrenot P, Bayle-Guillemaud P, and Villevieille C. Composite Electrode (LiNi0.6Mn0.2Co0.2O2) Engineering for Thiophosphate Solid-State Batteries: Morphological Evolution and Electrochemical Properties. ACS Energy Letters 2023;8:4957–65.

26. Payandeh S, Njel C, Mazilkin A, et al. The effect of single versus polycrystalline cathode particles on all-solid-state battery performance. Advanced materials interfaces 2023;10:2201806.

27. Self EC, Tsai WY, Westover AS, Browning KL, Yang G, and Nanda J. Benchmarking Solid-State Batteries Containing Sulfide Separators: Effects of Electrode Composition and Stack Pressure. Journal of the Electrochemical Society 2022;169:100510.

28. Nam JS, To A Ran W, Lee SH, et al. Densification and charge transport characterization of composite cathodes with single-crystalline LiNi0.8Co0.15Al0.05O2 for solid-state batteries. Energy Storage Materials 2022;46:155–64.

29. Strauss F, Bartsch T, De Biasi L, et al. Impact of Cathode Material Particle Size on the Capacity of Bulk-Type All-Solid-State Batteries. ACS Energy Letters 2018;3:992–6.

30. Shi T, Tu Q, Tian Y, et al. High Active Material Loading in All-Solid-State Battery Electrode via Particle Size Optimization. Advanced Energy Materials 2020;10.

31. Doerrer C, Capone I, Narayanan S, et al. High Energy Density Single-Crystal NMC/Li6PS5Cl Cathodes for All-Solid-State Lithium-Metal Batteries. ACS applied materials & interfaces 2021;13:37809–15.

32. Nakamura H, Kawaguchi T, Masuyama T, et al. Dry coating of active material particles with sulfide solid electrolytes for an all-solid-state lithium battery. Journal of power sources 2020;448.

33. Kim T, Ono LK, and Qi Y. Understanding the active formation of a cathode–electrolyte interphase (CEI) layer with energy level band bending for lithium-ion batteries. Journal of materials chemistry. A, Materials for energy and sustainability 2023;11:221–31.

34. Li W, Dolocan A, Oh P, et al. Dynamic behaviour of interphases and its implication on high-energy-density cathode materials in lithium-ion batteries. Nature communications 2017;8:14589.

35. Xu L, Tang S, Cheng Y, et al. Interfaces in solid-state lithium batteries. Joule 2018;2:1991–2015.

36. Kim J, Lee W, Seok J, et al. Inhomogeneous lithium-storage reaction triggering the inefficiency of all-solid-state batteries. Journal of Energy Chemistry 2021;66:226–36.

37. Liu X, Zheng B, Zhao J, et al. Electrochemo-Mechanical Effects on Structural Integrity of Ni-Rich Cathodes with Different Microstructures in All Solid-State Batteries. Advanced Energy Materials 2021;11.

38. Zhang W, Richter FH, Culver SP, et al. Degradation Mechanisms at the Li10GeP2S12/LiCoO2 Cathode Interface in an All-Solid-State Lithium-Ion Battery. ACS applied materials & interfaces 2018;10:22226–36.

39. Li X, Ren Z, Norouzi Banis M, et al. Unravelling the Chemistry and Microstructure Evolution of a Cathodic Interface in Sulfide-Based All-Solid-State Li-Ion Batteries. ACS Energy Letters 2019;4:2480–8.

40. Li X, Jin L, Song D, et al. LiNbO3-coated LiNi0.8Co0.1Mn0.1O2 cathode with high discharge capacity and rate performance for all-solid-state lithium battery. Journal of materials chemistry. A, Materials for energy and sustainability 2020;40:39–45.

41. Deng S, Li X, Ren Z, et al. Dual-functional interfaces for highly stable Ni-rich layered cathodes in sulfide all-solid-state batteries. Energy Storage Materials 2020;27:117–23.

42. Cao D, Zhang Y, Nolan AM, et al. Stable Thiophosphate-Based All-Solid-State Lithium Batteries through Conformally Interfacial Nanocoating. Nano letters 2020;20:1483–90.

43. Zhang J, Zheng C, Li L, et al. Unraveling the Intra and Intercycle Interfacial Evolution of Li6PS5Cl-Based All-Solid-State Lithium Batteries. Advanced Energy Materials 2020;10.

44. Neumann A, Randau S, Becker-Steinberger K, et al. Analysis of Interfacial Effects in All-Solid-State Batteries with Thiophosphate Solid Electrolytes. ACS applied materials & interfaces 2020;12:9277–91.

45. Otoyama M, Sakuda A, Tatsumisago M, and Hayashi A. Sulfide Electrolyte Suppressing Side Reactions in Composite Positive Electrodes for All-Solid-State Lithium Batteries. ACS applied materials & interfaces 2020;12:29228–34.

46. Marchini F, Saha S, Alves Dalla Corte D, and Tarascon JM. Li-Rich Layered Sulfide as Cathode Active Materials in All-Solid-State Li-Metal Batteries. ACS applied materials & interfaces 2020;12:15145–54.

47. Jiang W, Fan X, Zhu X, et al. Well-dispersed single-crystalline nickel-rich cathode for long-life high-voltage all-solid-state batteries. Journal of power sources 2021;508.

48. Lee JS and Park YJ. Comparison of LiTaO3and LiNbO3Surface Layers Prepared by Post-And Precursor-Based Coating Methods for Ni-Rich Cathodes of All-Solid-State Batteries. ACS applied materials & interfaces 2021;13.

49. Negi RS, Minnmann P, Pan R, et al. Stabilizing the Cathode/Electrolyte Interface Using a Dry-Processed Lithium Titanate Coating for All-Solid-State Batteries. Chemistry of materials: a publication of the American Chemical Society 2021;33:6713–23.

50. Morino Y and Kanada S. Electrochemical and material analyses for sulfide-based solid electrolyte–cathode interface under high voltage. Journal of power sources 2021;509.

51. Kim MJ, Choi IH, Jo SC, et al. A Novel Strategy to Overcome the Hurdle for Commercial All-Solid-State Batteries via Low-Cost Synthesis of Sulfide Solid Electrolytes. Small Methods 2021;5.

52. Wu L, Zhang Z, Liu G, Weng W, Zhang Z, and Yao X. Wet-Milling Synthesis of Superionic Lithium Argyrodite Electrolytes with Different Concentrations of Lithium Vacancy. ACS applied materials & interfaces 2021;13:46644–9.

53. Choi S, Yun BN, Jung WD, et al. Tomographical analysis of electrochemical lithiation and delithiation of LiNi 0.6 Co 0.2 Mn 0.2 O 2 cathodes in all-solid-state batteries. Scripta materialia 2019;165:10–14.

54. Sun Z, Lai Y, Lv N, et al. Insights on the Properties of the O-Doped Argyrodite Sulfide Solid Electrolytes (Li6PS5- xClOx,x=0-1). ACS applied materials & interfaces 2021;13:54924–35.

55. Park SW, Choi HJ, Yoo Y, et al. Stable Cycling of All-Solid-State Batteries with Sacrificial Cathode and Lithium-Free Indium Layer. Advanced functional materials 2022;32.

56. Peng L, Chen S, Yu C, et al. Unraveling the crystallinity on battery performances of chlorine-rich argyrodite electrolytes. Journal of power sources 2022;520.

57. Park C, Lee S, Kim K, Kim M, Choi S, and Shin D. Electrochemical Properties of Composite Cathode Using Bimodal Sized Electrolyte for All-Solid-State Batteries. Journal of the Electrochemical Society 2019;166:A5318–A5322.

58. Doux JM, Nguyen H, Tan DHS, et al. Stack Pressure Considerations for Room-Temperature All-Solid-State Lithium Metal Batteries. Advanced Energy Materials 2020;10.

59. Wang C, Yu R, Hwang S, et al. Single crystal cathodes enabling high-performance all-solid-state lithium-ion batteries. Energy Storage Materials 2020;30:98–103.

60. Phuc NHH, Morikawa K, Mitsuhiro T, Muto H, and Matsuda A. Synthesis of plate-like Li3PS4 solid electrolyte via liquid-phase shaking for all-solid-state lithium batteries. Ionics 2017;23:2061–7.

61. Tsukasaki H, Mori Y, Otoyama M, et al. Crystallization behavior of the Li2S-P2S5 glass electrolyte in the LiNi1/3Mn1/3Co1/3O2 positive electrode layer /639/638/675 /639/301/299/891 article. Scientific reports 2018;8.

62. Hikima K, Huy Phuc NH, and Matsuda A. Synthesis of 3Li2S–1P2S5–xLiI solid electrolytes by liquid-phase shaking method for all-solid-state Li metal batteries. Journal of Sol-Gel Science and Technology 2022;101:16–23.

63. Wu EA, Jo C, Tan DHS, et al. A Facile, Dry-Processed Lithium Borate-Based Cathode Coating for Improved All-Solid-State Battery Performance. Journal of the Electrochemical Society 2020;167:130516.

64. He ZY, Zhang ZQ, Yu M, et al. Synthetic optimization and application of Li-argyrodite Li 6 PS 5 I in solid-state battery at different temperatures RARE METALS. Rare Metals 2022;41:798–805.

65. Li H, Zhang T, Yang Z, Shi Y, Zhuang Q, and Cui Y. Electrochemical Impedance Spectroscopy Study on Using Li10GeP2S12 Electrolyte for All-Solid-State Lithium Batteries. International Journal of Electrochemical Science 2021;16:1–13.

66. Kitsche D, Tang Y, Hemmelmann H, et al. Atomic Layer Deposition Derived Zirconia Coatings on Ni-Rich Cathodes in Solid-State Batteries: Correlation Between Surface Constitution and Cycling Performance. Small Science 2023;3.

67. Cao D, Sun X, Li Y, Anderson A, Lu W, and Zhu H. Long-Cycling Sulfide-Based All-Solid-State Batteries Enabled by Electrochemo-Mechanically Stable Electrodes. Advanced materials 2022;34.

68. Zhang Q, Bruck AM, Stavola AM, Liang W, Aurora P, and Gallaway JW. Enhanced Electrochemical Stability of Sulfide-Based LiNi0.8Mn0.1Co0.1O2 All-Solid-State Batteries by Ti Surface Doping. Batteries and Supercaps 2021;4:529–35.

69. Liang J, Zhu Y, Li X, et al. A gradient oxy-thiophosphate-coated Ni-rich layered oxide cathode for stable all-solid-state Li-ion batteries. Nature communications 2023;14.

70. Park Y, Chang JH, Oh G, et al. Enhanced Electrochemical Stability and Extended Cycle Life in Sulfide-Based All-Solid-State Batteries: The Role of Li10SnP2S12 Coating on Ni-Rich NCM Cathode. Small 2023.

71. Zou C, Zang Z, Tao X, et al. Stabilized Cathode/Sulfide Electrolyte Interface through Conformally Interfacial Nanocoating for All-Solid-State Batteries. ACS Applied Energy Materials 2023;6:3599–607.

72. Liu X, Cheng Y, Su Y, et al. Revealing the surface-to-bulk degradation mechanism of nickel-rich cathode in sulfide all-solid-state batteries. Energy Storage Materials 2023;54:713–23.

73. Phuc NHH, Maeda T, Yamamoto T, Muto H, and Matsuda A. Preparation of Li3PS4–Li3PO4 Solid Electrolytes by Liquid-Phase Shaking for All-Solid-State Batteries. Electronic Materials Letters 2021;2:39–48.

74. Ren HT, Zhang ZQ, Zhang JZ, et al. Improvement of stability and solid-state battery performances of annealed 70Li2S–30P2S5 electrolytes by additives. Rare Metals 2022;41:106–14.

75. He ZY, Zhang ZQ, Yu M, et al. Synthetic optimization and application of Li-argyrodite Li6PS5I in solid-state battery at different temperatures. Rare Metals 2022;41:798–805.

76. Wang C, Hwang S, Jiang M, et al. Deciphering interfacial chemical and electrochemical reactions of sulfide-based all-solid-state batteries. Advanced energy materials 2021;11:2100210.

Data Availability

Main Text
Data for this article, including the electrochemistry and X-ray diffraction data shown here, is available at Harvard Dataverse at https://doi.org/10.7910/DVN/RET3CV.

Supplemental Information
Data for this Supplemental Information, including the electrochemistry shown here, is available at Harvard Dataverse at https://doi.org/10.7910/DVN/SGJAVW.